

Dynamics and instabilities of Lasing Light Bullets in Passively Mode-Locked Semiconductor Lasers

S. V. Gurevich*

*Institute for Theoretical Physics, University of Münster,
Wilhelm-Klemm-Str. 9, D-48149 Münster, Germany*

J. Javaloyes

Departament de Física, Universitat de les Illes Balears, C/ Valldemossa km 7.5, 07122 Mallorca, Spain

Recently, the existence of robust three-dimensional light bullets (LBs) was predicted theoretically in the output of a laser coupled to a distant saturable absorber. In this manuscript, we analyze the stability and the range of existence of these dissipative localized structures and provide guidelines and realistic parameter sets for their experimental observation. In order to reduce the complexity of the analysis, we first approximate the three-dimensional problem by a reduced equation governing the dynamics of the transverse profile. This effective theory provides an intuitive picture of the LB formation mechanism. Moreover, it allows us to perform a detailed multi-parameter bifurcation study and to identify the different mechanisms of instability. It is found that the LBs experience dominantly either homogeneous oscillation or symmetry breaking transversal waves radiation. In addition, our analysis reveals several non-intuitive scaling behaviors as functions of the linewidth enhancement factors and the saturation parameters. Our results are confirmed by direct numerical simulations of the full system.

I. INTRODUCTION

Light bullets (LBs) consists in pulses of light that are simultaneously confined in the transverse and the propagation directions. In the context of dissipative systems, LBs can be considered as Localized States (LSs) and are thus attractors of the dynamics. These hypothetical objects attracted a lot of interest in the last twenty years, both for fundamental and practical reasons. In practice, LBs should be addressable, i.e., they could be individually turned on and off, and one can envision that they would circulate indefinitely within an optical cavity as elementary bits of information.

Traditionally, the optical confinement scenario that would lead to LBs is envisioned through a conservative mechanisms in which a self-focusing nonlinearity compensates for the spreading effect of chromatic dispersion and/or diffraction. Seminal works demonstrated however that if the number of spatial dimensions is too large ($d_{\perp} \geq 2$), LBs are unstable and collapse [1], which was a result earlier discovered in the field of plasma physics [2]. Other confinement mechanisms were envisioned in forced dissipative system and LBs were predicted in optical parametric oscillators [3] and bistable cavities [4–6] with instantaneous nonlinearities.

Recently, a regime of temporal localization was predicted and experimentally demonstrated in a semiconductor passively mode-locked laser [7]. Passive mode-locking (PML) is a well known method for achieving short optical pulses [8]. It is achieved by combining two elements, a laser amplifier providing gain and a nonlinear

loss element, usually a saturable absorber. For proper parameters, this combination leads to the emission of temporal pulses much shorter than the cavity round-trip τ . It was shown in [7] that, if operated in the long cavity regime, the PML pulses become individually addressable temporal LSs coexisting with the off solution. In this long cavity regime, the round-trip time τ is made much longer than the semiconductor gain recovery time $\tau_g \sim 1$ ns, which is slowest variable. Interestingly, this temporal localization regime was found to be compatible with an additional spatial confinement mechanism, which lead to the theoretical prediction of a regime of stable three dimensional LBs [9].

While preliminary results based upon direct numerical integration allowed finding some basic estimates of the stability range for a generic parameter set, a full bifurcation study of the system described in [9] is still lacking. Yet, a multi-parameter analysis considering the various design factors of a passively mode-locked laser system would be of high relevance, in particular to experimental groups, as it would inform upon the proper parameter ranges in which an experimental realization may take place. In particular, assessing not only the range of existence of the LBs but also their destabilization mechanisms is of paramount importance. However, the LBs presented in [9] are particularly stiff multiple timescale objects in which the optical pulse is followed by a material “trail” that differs in extension by three orders of magnitudes. This stiffness, that occurs in the temporal domain or equivalently along the propagation axis, is exacerbated by the presence of the transverse dimensions that make a bifurcation analysis of two and three dimensional LBs a challenging problem.

We perform this analysis in this manuscript in two steps. Firstly, we approximate the solutions of the 3D problem by the product of a slowly evolving transverse

* gurevics@uni-muenster.de; Center for Nonlinear Science (CeNoS), University of Münster, Corrensstrasse 2, D-48149 Münster, Germany

profile and of a short pulse propagating inside the cavity. This allows us to obtain a reduced model governing the dynamics of the transverse profile. This effective theory allows to consider the LBs as if they were static diffractive spatial auto-solitons, similar, e.g., to those in [10]. We show that the transverse profile is governed by an effective Rosanov equation which allows for a detailed multi-parameter bifurcation study and also to identify the different mechanisms of instability. For that purpose, we employ the continuation and bifurcation package pde2path [19]. It is found that the light bullets experience dominantly either homogeneous oscillation or symmetry breaking lateral waves radiation. In addition, our analysis reveals several non-intuitive scaling behaviors as a functions of the linewidth enhancement factors and the saturation parameter. In the second stage, our predictions are confirmed by extensive direct numerical simulations of the spatio-temporal dynamics of the full system.

II. MODEL

We describe the passively mode-locked laser using the generic Haus partial differential equation (PDE) [8]. We consider a situation in which a broad area gain chip is coupled to a distant saturable absorber with telescopic optics in self-imaging conditions, as for instance in [12]. In this situation, each point of the gain section is mapped onto the absorber section and vice-versa. The diffraction in our system is the result from the propagation within the active sections. We assume that it is assumed sufficiently small as to justify the use of the paraxial approximation, as e.g. in [13]. We also work in the limit of moderate gain (G) and saturable absorption (Q) such that the uniform field limit applies. In this context, the equation governing the evolution of the field profile $E(r_\perp, z, \sigma)$ over the slow time scale σ reads

$$\partial_\sigma E = \left\{ \sqrt{\kappa} \left[1 + \frac{1 - i\alpha}{2} G(r_\perp, z, \sigma) - \frac{1 - i\beta}{2} Q(r_\perp, z, \sigma) \right] - 1 + \frac{1}{2\gamma^2} \partial_z^2 + (d + i) \Delta_\perp \right\} E(r_\perp, z, \sigma), \quad (1)$$

where γ is the bandwidth of the spectral filter representing, e.g., the resonance of a VCSEL [14], $\Delta_\perp = \partial_x^2 + \partial_y^2$ is the transverse Laplacian, κ is the fraction of the power remaining in the cavity after each round-trip and α and β are the linewidth enhancement factors of the gain and absorber sections, respectively. The amount of diffraction in the combined gain and absorber sections can be described by a diffraction length that was used in Eq.(1) to normalize the transverse space variables $r_\perp = (x, y)$. As such, the transverse domain size L_\perp becomes a bifurcation parameter. For small L_\perp , the system is governed by its transverse boundary conditions and conversely, localized states may occur when $L_\perp \gg 1$. The parameter d represents the small amount of field diffusion incurred for instance by the dependence of the reflectivity of the

VCSEL distributed Bragg Reflectors upon the angle of incidence. The longitudinal variable (z) is identified as a fast time variable and represents the evolution of the field within the round-trip. The carrier dynamics read

$$\partial_z G = \Gamma G_0 - G \left(\Gamma + |E|^2 \right) + \mathcal{D}_g \Delta_\perp G, \quad (2)$$

$$\partial_z Q = Q_0 - Q \left(1 + s |E|^2 \right) + \mathcal{D}_q \Delta_\perp Q, \quad (3)$$

with G_0 the pumping rate, $\Gamma = \tau_g^{-1}$ the gain recovery rate, Q_0 is the value of the unsaturated losses, s the ratio of the saturation energy of the gain and of the SA sections and $\mathcal{D}_{g,q}$ the scaled diffusion coefficients. In general, the non-instantaneous and causal response of the active medium represented by the variable G implies a lack of parity along (z) for the LSs generated by Eqs. (1-3), see [15] for details. In Eqs.(1-3) the fast time (z) has been normalized to the SA recovery time that we assume to be $\tau_{sa} = 20$ ps. Setting $\gamma = 40$ and $\Gamma = 0.04$, corresponds to a full Width at Half Maximum of 250 GHz for the gain bandwidth and a carrier recovery time $\tau_g = 500$ ps. Assuming a diffraction length of $l_\perp = 1 \mu\text{m}$ and a domain size $L_\perp = 190$ corresponds to a $190 \mu\text{m}$ broad area device. The typical dimensions of the LB are $l_{LB} \sim 10 \mu\text{m}$ and $\tau_{LB} \sim 4$ ps. Finally, it was shown in [9] that carrier diffusion plays almost no role in the dynamics, so that we set the diffusion coefficients $\mathcal{D}_{g,q} = 0$. For proper system parameters, Eqs. (1-3) sustain the existence of stable three-dimensional light bullets as depicted in Fig. 1. The details regarding the numerical method used to solve Eqs. (1-3) can be found in Section 4 of the Appendix.

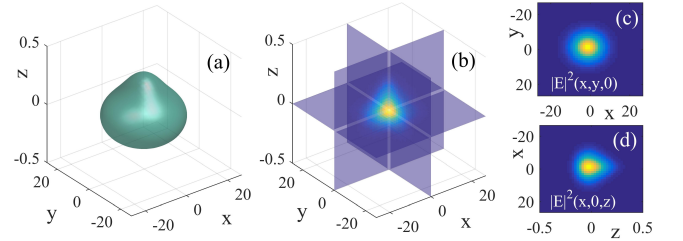


Figure 1. (Color online) Exemplary solutions of Eqs. (1-3) showing the intensity profile of a stable LB. (a) Isosurface at 1% of the maximal value. (b) Cross-sections in the three orthogonal planes defined as $x = 0$, $y = 0$ and $z = 0$. The corresponding cross-section profiles are presented in the insets (c) and (d). Parameters are $(\gamma, \kappa, \alpha, \beta, \Gamma, G_0, Q_0, s, d) = (40, 0.8, 1.5, 0.5, 0.04, 0.425, 0.354, 30, 10^{-2})$.

Exploiting the seminal work of New [16] and the fact that the LBs are composed of variables evolving over widely different timescales, one can find an approximate model governing the shaping of the transverse profile. We assume that the field reads $E(r_\perp, z, \sigma) = A(r_\perp, \sigma) p(z)$ with $p(z)$ a short normalized temporal pulse of length τ_p that represents the temporal LS upon which the LB is built and $A(r_\perp, \sigma)$ is a slowly evolving amplitude. Separating the temporal evolution into the fast and slow parts

corresponding to the pulse emission and the subsequent gain recovery allows us to find the equation governing the dynamics of A as

$$\partial_t A = (d + i) (\partial_u^2 + \partial_v^2) A + f(|A|^2) A. \quad (4)$$

Defining $h(P) = (1 - e^{-P})/P$, $P = |A|^2$ the function f reads

$$f(P) = (1 - i\alpha)g(1 + q)h(P) - (1 - i\beta)qh(sP) - 1 \quad (5)$$

see Section 1 of the Appendix for more details. We defined in Eqs. (4,5) the scaled spatial and temporal coordinates as $t = (1 - \sqrt{\kappa})\sigma$ and $(u, v) = \sqrt{1 - \sqrt{\kappa}}(x, y)$. The effective parameters that are the gain normalized to threshold g and the normalized absorption q as $g = G_0/G_{th}$ and $q = Q_0/(\frac{2}{\sqrt{\kappa}} - 2)$. We defined $G_{th} = \frac{2}{\sqrt{\kappa}} - 2 + Q_0$ as the threshold gain value above which the off solution $(E, G, Q) = (0, G_0, Q_0)$ becomes unstable. All the localized states are found below the threshold for which $G < G_{th}$ or equivalently $g < 1$. We note that in the representation given in Eqs. (4,5) in which the threshold is automatically unity, the only parameters that appear are (g, q, α, β, s) as the cavity losses κ have been factored out. Note however that Eqs. (1-3) are obtained in the limit of small gain and losses. A too strong departure from the good cavity limit would necessitate larger gain which would induce additional nonlinearities. Here, the losses could not be factored out anymore.

Interestingly, the equation (4) governing the dynamics of the transverse profile is a so-called Rosanov equation [10, 22] that is known in the context of static transverse auto-solitons in bistable interferometer. In these works one assumes a monomode continuous wave (CW) emission along the longitudinal propagation direction which allows, via the adiabatic elimination of the material variables, to find an effective equation for the transverse profile. The nonlinear function $h(P)$ would correspond to a static saturated nonlinearity, i.e. $h(P) \rightarrow 1/(1 + P)$. A similar result can be obtained setting $\partial_z G = \partial_z Q = 0$ in Eqs. (1-3). However, the adiabatic approximation of the gain along the propagation direction would be incorrect for a semiconductor material and the reaction time of the gain is known to profoundly affect the stability of spatio-temporal structures [6].

We note that we operate in a parameter regime where the function $f(P)$ possesses two fixed points. One solution is unstable and corresponds to a lower intensity temporal LS while the stable fixed point corresponds to a higher intensity LS. As such, the system is not bistable for the CW solution, preventing the existence of static transverse auto-solitons. It is however bistable for the amplitude of the temporal LS whose spatial profile may, for proper parameters, coalesce into a transverse soliton. In the following, we will call the homogeneous spatial solution the temporal LS with an uniform spatial profile.

Spatial LSs can be found within the region of bistability of the homogeneous solution. As such, studying in

which conditions the homogeneous solutions of Eqs. (4,5) develops a hysteresis region informs on the proper parameters for spatial localization. This analysis is performed in Section 2 of the Appendix, see in particular Fig. 8 and Fig. 9. We summarize here our main results. The critical value of q_c above which one obtain a sub-critical region as a function of the normalized gain g reads $q_c = 1/(s_c - 1)$. In presence of a sub-critical region, the folding point, i.e. the minimal value for the gain g_m for which one can obtain a non-zero solution (see for instance the lower red circle in Fig. 2a)) can be approximated by

$$g_m = -\frac{W_{-1}(-e^{-1-\frac{q}{s}})}{1 + q} \quad (6)$$

with the Lambert-W function W_n . The extent of the sub-critical region in which one may expect spatial LSs is then $g \in [g_m, 1]$. The asymptotics in the limit of large saturation and large absorption simply read

$$\lim_{s \rightarrow \infty} g_m = \frac{1}{1 + q}, \quad \lim_{q \rightarrow \infty} g_m = \frac{1}{s}. \quad (7)$$

Our results indicate that large modulations of the absorber q and large saturation parameters s of course favor the breadth of a sub-critical region, in agreement with intuition. However, less intuitive is that a saturation effect exists and marginal increases of the bistability domain are found for $s > 20$ and $q > 2$, see Fig. 2 in Section 2 of the appendix for more details on the evolution of the folding point.

III. RESULTS

The single LS solutions of Eqs. (4,5) can be found in the form

$$A(u, v, t) = a(u, v) e^{-i\omega t}, \quad (8)$$

where $a(u, v)$ is a complex amplitude with the localized field intensity $P = |a|^2$ and ω that represents the carrier frequency of the solution. Substituting Eq. 8 into Eqs. (4,5) we are left searching for unknowns a and ω of the following equation

$$(d + i) (\partial_u^2 + \partial_v^2) a + i\omega a + f(|a|^2) a = 0. \quad (9)$$

To directly track the LS solutions of Eq. (9) in parameter space, we make use of pde2path [19, 23], a numerical pseudo-arc-length bifurcation and continuation package for systems of elliptic partial differential equations. Details regarding the numerical implementation of the problem can be found in Section 3 of the appendix.

Evolution of the folding point of the LS solution As mentioned, the LS branch also possesses a folding point, see for instance the blue circle denoted SN in Fig. 2 which represents the minimal value of the gain at which localized states can be obtained. The analysis of the primary

folding point of the LS branch g_{SN} as a function of the normalized absorption q and the saturation parameter s is detailed in Section 3 of the appendix. It is found that g_{SN} follows closely the evolution of the folding point of the uniform solution g_m with q and s , compare Fig. 9 and Fig. 10 in Sections 2 and 3 of the appendix, respectively. That is, our predictions for the evolution of the folding point of the homogeneous solution hold also for the LS branch and our approximate analytical expression can be used as a guideline. The one-dimensional folding point is always shifted a few percent toward higher current values as compared to the uniform case, see Fig. 2a,b) and compare the red and blue curves. A similar shift for the two-dimensional case exists with respect to the one dimensional situation, see Fig. 10 in Section 3 of the appendix.

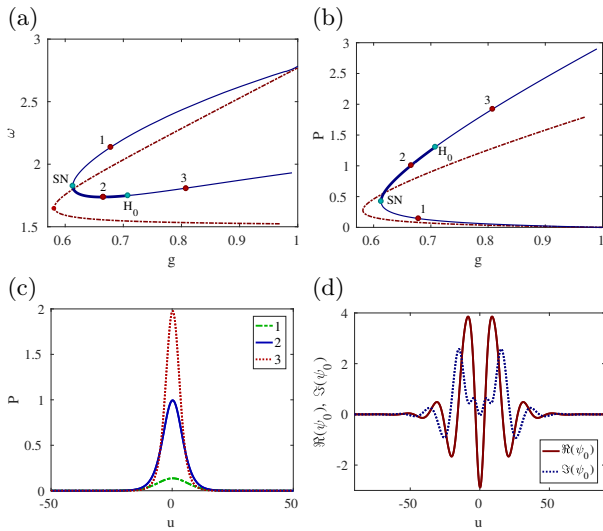


Figure 2. (Color online) Comparison between the behavior of the branch of the single LS solution (solid blue line) with that of the homogeneous solution (red dash-dotted line) calculated for $\alpha = 1.5$, $\beta = 0.5$. The evolution of (a) the spectral parameter ω and (b) the (peak) intensity P as a function of the normalized gain g is presented. Three exemplary stationary LS profiles existing for different values of g are depicted in (c). The LS is stable between the saddle-node bifurcation point SN and the Andronov-Hopf bifurcation point H_0 (thick blue line). We show the real (solid red line) and imaginary (dashed blue line) parts of the corresponding critical eigenfunction ψ_0 in (d). Other parameters are: $q = 1.27$, $s = 30$, $d = 0.01$.

Bifurcation analysis in one dimension We now turn our attention to the possible mechanisms of instability occurring for increased values of the gain and we present in Fig. 2 the bifurcation diagram of Eq. 9 as a function of g calculated for $\alpha = 1.5$ and $\beta = 0.5$. In particular, Fig. 2 (a) represents the spectral parameter ω of the homogeneous solution (red dash-dotted line) and that of the one-dimensional LS (solid blue line) as a function of the gain g , while the power P as a function of g for both homogeneous (dash-dotted red line) and LS solutions (solid

blue line) is depicted in Fig. 2 (b). In the case of the LS we plot the peak intensity of the solution. We note that the bistability range of the single LS solution is contained in that of the homogeneous one. In addition, in Fig. 2 (c) we depict three exemplary stationary LS profiles existing for different values of g as indicated by enumerated labels in both panels (a,b). The power of the LS changes significantly along the branch, leading to a formation of narrow peaks of high intensity at the upper power branch.

Apart from the overall information regarding the branch morphology, the linear stability of a particular LS solution along the branch can be obtained directly during continuation. The stability analysis of Eqs. (4,5) reveals the existence of several neutral eigenvalues, corresponding to the translation, phase and Galilean invariances (cf. Refs. [24, 25] for static auto-solitons). The results of the linear stability analysis are shown in Fig. 2 (a), (b). Here, thick (thin) blue curves correspond to stable (unstable) LS solutions. The LS stability domain lies between the saddle-node bifurcation point SN and the Andronov-Hopf (AH) bifurcation point H_0 . There, the branch of LS gets destabilized via symmetric oscillations, i.e. a breathing of the LS profile, see [video1](#). An example of the real (solid red line) and imaginary (dashed blue line) parts of the critical eigenfunction ψ_0 associated to this breathing instability is shown in Fig. 2 (d).

We note that it was shown in [9] that, similar to the case of static autosolitons [22, 24], the branch of one-dimensional LS forms a spiral in the (g, ω) plane for vanishing linewidth enhancement factors of both gain and absorber sections. We show here that, for more realistic values of (α, β) , one finds a simpler branch structure that possesses a single fold. Our analysis of the evolution of the spiral structure of the branch and of the spectral parameter ω as a function of the gain g for small values of (α, β) can be found in Section 3, Fig. 11 of the appendix. We also note that for these more realistic values of (α, β) the breadth of the stable region is more extended $\Delta g = g_{H_0} - g_{SN} \sim 0.1$ while $\Delta g \sim 0.03$ in [9]. This results indicates that the range of stable LB existence can be widely improved by a proper design of the experimental devices.

Bifurcation analysis in two dimensions We performed a similar analysis in two transverse dimensions obtained for fixed values of $\alpha = 1.7$ and $\beta = 0.5$. Our results are presented in Fig. 3, where the dependence of evolution of the spectral parameter ω (panel (a)) and the peak intensity P (panel (b)) on the gain g is shown. Note that the overall morphology of the two-dimensional LS branch resembles the one-dimensional behavior (cf. Fig. 2). However, it turns out that a richer dynamics occurs and that additional modes of instability are found in two transverse dimensions. Besides a symmetrical radiation mode, see Fig. 3 (c) leading to an Andronov-Hopf bifurcation, similar to the one dimensional case and also noted H_0 , compression-elongation oscillations in the two orthogonal directions are also possible, see Fig. 3 (d), which correspond to a bifurcation point noted H_2 . By

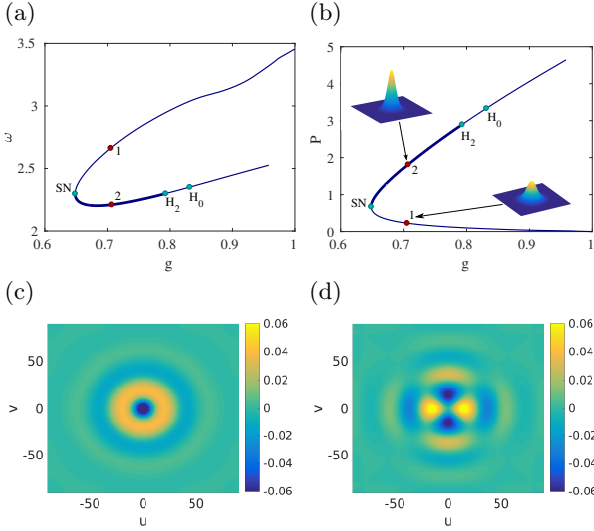


Figure 3. (Color online) Bifurcation diagram for a two-dimensional LS obtained for $\alpha = 1.7$, $\beta = 0.5$ as a function of the gain g , showing the evolution of (a) the spectral parameter ω while the peak intensity P is depicted in (b). The LS is stable between the saddle-node bifurcation point SN and the AH bifurcation point H_2 (thick blue line). The secondary AH bifurcation point is indicated as H_0 . Two insets in Fig. 3 (b) show intensity profiles, corresponding to an unstable (label 1) and a stable (label 2) LS solution obtained at the same gain value $g = 0.705$. We show the real parts of both $n = 0$ and $n = 2$ critical modes calculated at $g = 0.68$ in (c), (d), respectively. Other parameters are the same as in Fig. 2.

defining the polar angle ϕ in the transverse plane, we can summarize the situation by saying that the point spectrum of the two-dimensional LS contains modes $\propto e^{in\phi}$ with $n = 0, \pm 2$. The mode with $n = 0$ results in a symmetrical change of the size of the LS and $n = \pm 2$ correspond to a deformation of the LS in two perpendicular directions. Figure 3 (c), (d) show real parts of both $n = 0$ (panel (c)) and $n = 2$ (panel (d)) critical modes.

Our linear stability analysis indicates that similar to the one-dimensional case, the LS solution appears in a saddle-node bifurcation (SN) at low gain while at high current the dominant mechanism of instability consists in an AH bifurcation at the point H_2 , where the corresponding $n = \pm 2$ modes become unstable, see [video2](#). That is, thick (thin) blue curve in Fig. 3 (a), (b) corresponds to stable (unstable) LS. In addition, two insets in Fig. 3 (b) show intensity distributions, corresponding to an unstable (label 1) and a stable (label 2) part of the LS branch obtained at the same gain value $g = 0.705$. Finally, the AH bifurcation point H_0 indicates a secondary instability of the LS w. r. t. modes with $n = 0$, see [video3](#). Here, additional symmetrical oscillations of the LS shape are expected. Notice that the order of both AH bifurcations strongly depends on the linewidth enhancement factors of both gain and absorber sections.

Range of existence of the single LS. In [9], the linewidth enhancement factors of both the gain and ab-

sorber sections were set $\alpha = \beta = 0$ as a demonstration that the carrier induced self-focusing effects played no role in the LB formation and that the confinement mechanism was different than the one found in conservative systems as, e.g., in [1]. In this section, we study the influence of the α and β factors that are set to more typical values and we find that an extended range of stability exists by mapping the position of the points H_0 and H_2 limiting the existence of stable LBs at high current. Adding to these results the evolution of the folding point SN, allows us to disclose the range of existence of stable LSs in one and two transverse spatial dimensions.

As we mentioned above, in the one-dimensional case, at high current the dominant mechanism of instability consists in an Andronov-Hopf bifurcation H_n with $n = 0$, whereas in the two-dimensional case we identified several modes of destabilization, where the amplitude of the LS oscillates uniformly in space ($n = 0$) and another where the breadth of the LS breathes ($n = 2$). In order to study the influence of the α and β factors on the stability range of the single LS solution we perform a two parameter continuation of the fold and AH bifurcation points as a function of the gain g and the linewidth enhancement factors of the gain and the absorber sections. Our results are depicted in Fig. 4.

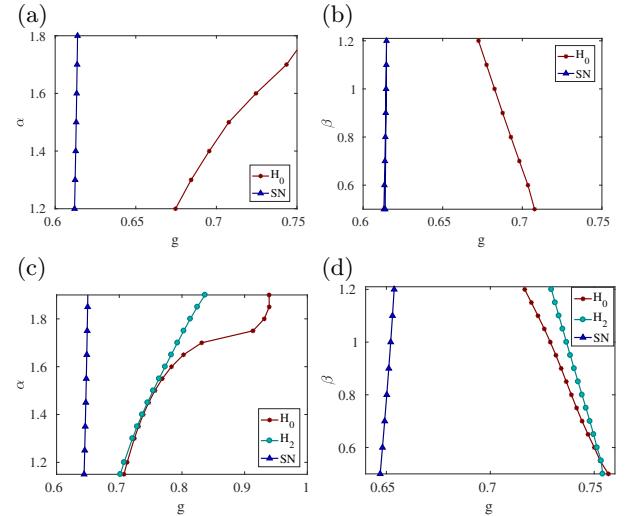


Figure 4. (Color online) (a), (b). One-dimensional stability diagrams showing the threshold for the fold (blue triangles) and $n = 0$ AH bifurcations (red stars) in terms of the dependence of α on the gain g for (a) $\beta = 0.5$ and (b) $\alpha = 1.5$. (c), (d). The same stability diagram in two dimensions. Cyan circles depict the Hopf line corresponding to the $n = 2$ instability. The range of stability grows with α and shrinks with β .

Figure 4 panels (a), (c) represent the stability diagrams in the (g, α) plane for the fixed value of $\beta = 0.5$ for one and two spatial dimensions, respectively. Here, blue triangles indicate the fold threshold, whereas red stars stand for the boundary of the AH bifurcation with $n = 0$. In addition, in Fig. 4 (c) cyan circles depict the second AH

line $n = 2$. Note that depending on the relation between α and β one of these two oscillation modes can govern the primary instability threshold. Our results reveal that in both one and two dimensions the range of the stability increases toward higher α values. Although the fold position keeps almost constant for increasing α , both AH lines move toward higher currents. However, the width of the stability region strongly depends on β as shown in Fig. 4 (b), (d), where the stability diagram for increasing β and a fixed moderate value of $\alpha = 1.5$ is presented for both one- and two-dimensional continuations. Here, in both cases the range of stability decreases for growing β .

Finally, we performed a similar analysis as a function of the saturation parameter s as shown in Fig. 5. One notices that for generic values of $(\alpha, \beta) = (1.5, 0.5)$, the stability region *decreases* if the saturation parameter s gets too large, which is a counter-intuitive result.

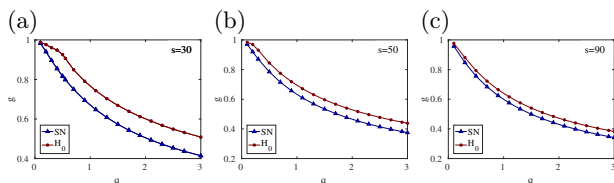


Figure 5. (Color online). One-dimensional stability diagrams showing the threshold for the fold (blue triangles) and the $n = 0$ AH bifurcations (red stars) in terms of the dependence of s on the gain g for $(\alpha, \beta) = (1.5, 0.5)$. The range of stability shrinks for too large values of s . Similar trends are found in two dimensions.

Numerical Simulations of the Haus model By using the guidelines obtained from the analysis of the homogeneous and the transverse solutions, we now turn our attention to the predictions obtained by directly integrating Eqs. (1-3), the details of the numerical methods are depicted in Section 4 of the appendix. Our results are summarized in Fig. 6 in which we plot the energy of the LB $\mathcal{E} = \iint |E|^2 dx dz$ and depict the region of stable existence as a function of the gain g and the linewidth enhancement factors α and β . Nicely, the dominant trends predicted by analyzing the effective equation of the transverse profile Eq. (4) are confirmed, a strong increase of the stable region with α , and a moderate decreases for increasing β . In [video4](#), we depict the instability mechanisms in 2D that corresponds to H_0 , as predicted, while in 3D, the dominant mechanism is governed by the H_2 instability [video5](#).

The transverse and longitudinal Full Width at Half Maximum (FWHM), the carrier frequency ω and drift speed v of the LBs are presented in Section 4 of the appendix.

A similar behavior as that predicted in Fig. 5 can be found while performing the integration of the Haus model in Eqs. (1-3) as a function of the saturation parameter s . Our results are summarized in Fig. 7 where we represented the energy, the other parameters of the solutions are depicted in Section 4 of the appendix. The domi-

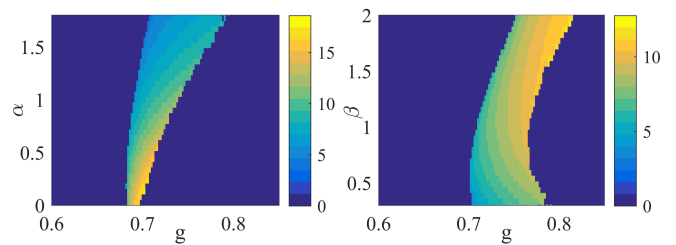


Figure 6. (Color online). Two-dimensional bifurcation diagram showing the region of stable existence of the LBs by integrating the two-dimensional Haus Equation in (x, z) as a function of the gain g and the parameters α (a) and β (b). The color code represents the energy of the LB \mathcal{E} . The range of stability increases with α and reduces for small values of β in agreement with Fig. 4. Similar trends were found in three dimensions. Parameters are $(\gamma, \kappa, \Gamma, Q_0, s, d) = (40, 0.8, 0.04, 0.3, 30, 10^{-2})$ and $\beta = 0.5$ (a), $\alpha = 1.5$ (b).

inant trends of a decrease of the region of existence with increased values of s is confirmed.

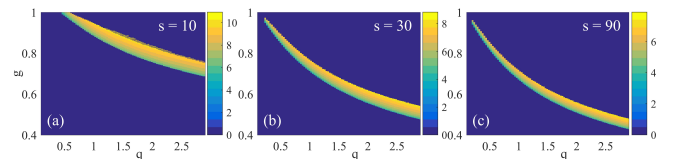


Figure 7. (Color online). Two-dimensional bifurcation diagram showing the region of stable existence of the LBs by integrating the two dimensional Haus Equation as a function of the gain g and the modulation of the absorption q . The color code represents the energy of the LB \mathcal{E} for increasing values of the saturation parameter s . We find that the range of stability decreases with increasing values of s . Similar trends were found in three dimensions. Parameters are $(\gamma, \kappa, \alpha, \beta, \Gamma, d) = (40, 0.8, 1.5, 0.5, 0.04, 10^{-2})$.

IV. CONCLUSION

In conclusion, we discussed how the dynamics of 3D light bullets can be successfully approximated in a wide parameter range by a simplified model governing the dynamics of the transverse profile. The bifurcation analysis of this effective model allows to obtain guidelines regarding the existence and the stability of the LBs found in the full problem. We have found that, as a function of the gain, the stability range is governed by the evolution of a lower limit point where the LB solution ceases to exist and an upper one where the system develops a breathing instability that can result either in a homogeneous oscillation of the profile or orthogonal compression-elongation oscillations. We have found that, contrary to intuition, too large saturation parameters or modulation of the losses are either detrimental or irrelevant to the range of stability of the LBs. Finally, direct numerical

simulations performed on a HPC cluster of the full system confirmed the predictions of the simplified model. In our analysis we have found that the mechanism of instability of the LBs are essentially those of the transverse profile. Yet, we believe that additional instabilities may take place for larger values of (α, β) for which the temporal LS that is performing the backbone of the spatial soliton can become unstable. Finally, instabilities that do not pertain to either the spatial or the temporal degree of freedom but to both simultaneously can not be ruled out and will be the topic of further studies.

ACKNOWLEDGMENTS

S.G. acknowledges the Universitat de les Illes Balears for funding a stay where part of this work was developed. J.J. acknowledges Joan Arbona for technical support regarding the UIB cluster Foner, the project COMBINA (TEC2015-65212-C3-3-P AEI/FEDER UE) and the Ramón y Cajal fellowship. J.J. and S.G. thanks Christian Schelte for a careful reading of the manuscript.

Appendix

1. Derivation of the Effective Rosanov Equation

We assume that the field reads $E(r_\perp, z, \sigma) = A(r_\perp, \sigma)p(z)$ with a short normalized temporal pulse $p(z)$ of length τ_p and a slowly evolving amplitude $A(r_\perp, \sigma)$. Next, we use the fact that, during the emission of a LB, the stimulated terms are dominant in Eqs.(2-3), i.e. $|E|^2 \gg 1$ such that

$$-\int_0^{\tau_p} G |E|^2 dz \simeq \int_0^{\tau_p} \partial_z G dz = G_f - G_i \quad (\text{A.1})$$

with G_i (resp. G_f) the gain before (resp. after) the pulse emission, see [16, 17] for more details. By integrating Eq. (2) in the regime $|E|^2 \gg 1$ we find that $G(z) = G(0) \exp\left(-\int_0^z |p|^2 |A|^2 dz'\right)$ and $G_f = G_i \exp\left(-|A|^2\right)$. Considering Eq. (3) with similar arguments one finds $Q_f = Q_i \exp\left(-s|A|^2\right)$. Multiplying the field equation Eq. (1) by \bar{p} , integrating over the pulse length, neglecting the contribution $\gamma^{-1}\dot{p}$, and using the above expression of the stimulated terms, we find that the equation governing the dynamics of the transverse profile reads

$$\partial_\sigma A = (d+i)\Delta_\perp A + A F\left(|A|^2\right). \quad (\text{A.2})$$

The expression of the nonlinear function F is

$$F = \sqrt{\kappa} \left[1 + \frac{1-i\alpha}{2} G_0 h(P) - \frac{1-i\beta}{2} Q_0 h(sP) \right] - \text{A.3}$$

with $h(P) = (1 - e^{-P})/P$. We replaced in Eq. (12) the values of the gain and of the absorption at the beginning

of the pulse by their equilibrium values by taking advantage of the long cavity limit. It allows us to assume that the gain and absorption loses entirely their memory at the next round-trip.

The lasing threshold above which the off solution $(E, G, Q) = (0, G_0, Q_0)$ becomes unstable is

$$G_{th} = \frac{2}{\sqrt{\kappa}} - 2 + Q_0. \quad (\text{A.4})$$

As we operate in the region below threshold in which the temporal LSs are bistable with the trivial off solution, we define the gain normalized to threshold and the normalized absorption q as

$$g = G_0/G_{th} \quad , \quad q = Q_0/\left(\frac{2}{\sqrt{\kappa}} - 2\right). \quad (\text{A.5})$$

Defining the scaled spatial and temporal coordinates as $t = (1 - \sqrt{\kappa}) \sigma$ and $(u, v) = \sqrt{1 - \sqrt{\kappa}}(x, y)$ yields the normalized equations

$$\partial_t A = (d+i)(\partial_u^2 + \partial_v^2) A + f(|A|^2) A, \quad (\text{A.6})$$

$$f(P) = (1-i\alpha)g(1+q)h(P) - (1-i\beta)qh(sP) - \text{A.7}$$

where we defined $F = f/(1 - \sqrt{\kappa})$ and $P = |A|^2$.

2. Behavior of the homogeneous solution

The monochromatic solutions of Eqs.(4-5) denoted as $A = \sqrt{P} \exp(-i\omega t)$ with $P \in \mathbb{R}$ are given by $\Re(F) = 0$ which yields the implicit relation between gain and power

$$g = \frac{1 + qh(sP)}{(1+q)h(P)}. \quad (\text{A.8})$$

As we consider the transverse profile of a LB, P actually corresponds to the power carried by the temporal LS and the multiple solutions of Eq. (17) are to be identified with temporal LSs with different power densities. Once P is known, the carrier frequency of the solution can be found independently solving

$$\omega = \alpha g(1+q)h(P) - \beta qh(sP). \quad (\text{A.9})$$

Super-subcritical transition point A simple Taylor expansion of Eq. (17) around the threshold gives the relation

$$g = 1 + p \frac{1+q(1-s)}{2(1+q)}. \quad (\text{A.10})$$

As such, the solution curve experiences a transition from super-critical toward sub-critical when

$$1 + q_c(1 - s_c) = 0. \quad (\text{A.11})$$

yielding a relation between the critical saturation s_c and the breadth of the absorber modulation q_c .

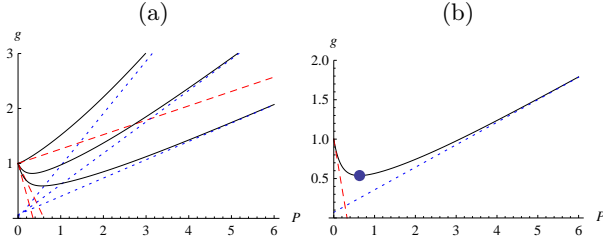


Figure 8. (a) Evolution of the bistability regime for $s = 10$ and increasing values of $q = 0.05, 0.75$ and 2 (black lines) and (b) Approximation of the folding point (P_m, g_m) for $s = 10$ and $q = 2.5$ (blue circle). In both cases the homogeneous solution is represented by a black line and the asymptotic expansions for low and high power are represented in dashed red and dotted blue lines, respectively.

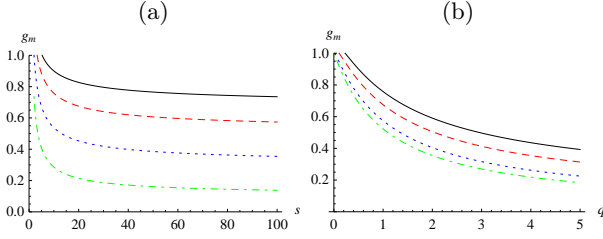


Figure 9. (a) Evolution of the approximation of the folding point as a function of s and different values of q that correspond to $q = 0.5$ (continuous) $q = 1$ (dashed red), $q = 2.5$ (dotted blue) and $q = 10$ (dash-dotted green) lines, respectively. (b) Evolution of the approximation of the folding point as a function of s and different values of q that correspond to $q = 0.5$ (continuous) $q = 1$ (dashed red), $q = 2.5$ (dotted blue) and $q = 10$ (dash-dotted green) lines, respectively.

High power branch The upper solution branch for which the values of P are large, can be approximated by replacing the nonlinear function $h(P)$ by its asymptotic value $h \sim 1/P$, such that Eq. (17) takes the form

$$g(P) \simeq \frac{P + \frac{q}{s}}{1 + q} \sim \frac{P}{1 + q} \quad (\text{A.12})$$

and where we used the large saturation approximation. The evolution of the solution from the super-critical toward the sub-critical regime is depicted in Fig. 8(a), in addition to the asymptotic regimes for low and high intensities.

Folding point approximation The folding point is achieved at powers at which the saturable absorber is saturated but the gain is not. We replace only $h(sP)$ by its high power expansion in Eq. (A.8) to find

$$g(P) = \frac{P + \frac{q}{s}}{(1 + q)(1 - e^{-P})}. \quad (\text{A.13})$$

Searching for the folding point as a minimum of $g(P)$ yields a solution P_m that is only a function of q/s and reads

$$P_m\left(\frac{q}{s}\right) = -1 - \frac{q}{s} - W_{-1}\left(-e^{-1-\frac{q}{s}}\right) \quad (\text{A.14})$$

with $W_n(z)$ the Lambert-W function. We define the value of the gain at the folding point as $g_m = g(P_m)$ as it is a measure of the extent of the sub-critical region

$$g_m = -\frac{W_{-1}\left(-e^{-1-\frac{q}{s}}\right)}{1 + q}. \quad (\text{A.15})$$

The accuracy of our approximation is depicted in Fig. 8(b) by a blue circle. One can see that it is indistinguishable from the exact value.

Finally, while the solution of Eq. (A.15) using the Lambert function is maybe complicated, the asymptotic values of g_m in the limit of large saturation and large absorption are simply

$$\lim_{s \rightarrow \infty} g_m = \frac{1}{1 + q}, \quad \lim_{q \rightarrow \infty} g_m = \frac{1}{s}. \quad (\text{A.16})$$

The scaling behavior of the folding point as a function s using Eq. A.15 are represented in Fig. 9(a). We note that the asymptotic behavior in Fig. 9(a) can only be obtained for very large values of s . Similarly, the curves in Fig. 9(b) converge toward $g_m = s^{-1}$ for unrealistically large values of q . However, the behavior predicted by Eq. (A.16) is qualitatively verified.

3. Bifurcation analysis of the Rosanov Equation

a. Numerical method

The LS solutions of Eqs.(4-5) can be found in the form $A(r, t) = a(r)e^{-i\omega t}$, where $r = (u, v)$ are normalized transverse spatial coordinates, $a(r)$ is the complex amplitude with the field intensity $P = |a|^2$ localized around some point in space and ω is the spectral parameter. To directly track LS solutions of Eq. (9) in the parameter space, we make use of pde2path [19, 23], a numerical pseudo-arc-length bifurcation and continuation package for systems of elliptic partial differential equations over bounded multidimensional domains which is based on the finite-element methods of Matlab's pde toolbox and OOPDE toolbox.

In general, path continuation procedures determine stationary solutions of a dynamical system combining prediction steps where a known steady state solution is advanced in parameter space via a tangent predictor and correction steps where Newton procedures are used to converge to the next solution at a new value of the primary continuation parameter [20, 21]. In this way one can start at, e.g., a numerically given solution, continue it in parameter space, and obtain a solution branch including its stability. The primary continuation parameter is in our case the gain parameter g , whereas the corresponding spectral parameter ω is used as an additional free parameter that is automatically adapted to the corresponding g during continuation. Further, one needs an additional auxiliary condition to break the phase shift symmetry of the system in question in order to prevent

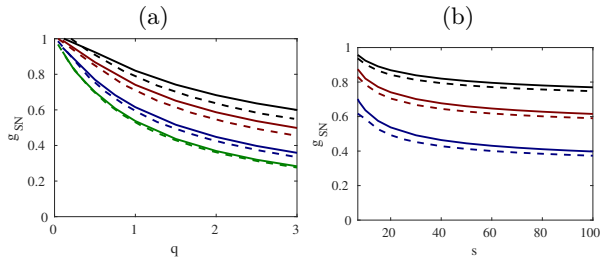


Figure 10. (Color online) (a) Continuation of the folding point g_{SN} of a single LS branch as a function of the normalized absorption q and different values of s that correspond to $s = 10$ (black) $s = 20$ (red), $s = 100$ (blue) and $s = 1000$ (green). (b) Continuation of g_{SN} of a single LS branch as a function of s and different values of q that correspond to $q = 0.5$ (black) $q = 1$ (red), $q = 2.5$ (blue) lines. Dashed (solid) lines in both panels indicate one- (two-) dimensional continuation, respectively.

the continuation algorithm to trivially follow solutions along the corresponding degree of freedom. This condition can be easily implemented by, e.g., setting the phase of the LS to zero in the center of the computational domain.

To increase computational efficiency in two dimensions, we exploit the rotational symmetry of the LS and only compute one quarter of the physical domain $\Omega_2 = [-L_u, L_u] \times [-L_v, L_v]$ with $L_u = L_v = 90$ using a grid with $N_u \times N_v$ mesh points, $N_u = N_v = 256$. As a result Neumann boundary conditions are imposed in both u, v directions, whereas periodic boundary conditions are employed in the one-dimensional case. There, the continuation is performed on the one-dimensional domain $\Omega_1 = [-L_u, L_u]$ with $L_u = 90$ using $N_u = 512$ equidistant mesh points.

b. Evolution of the folding point of the LS with q and s

In this section we discuss the influence of the system parameters, e.g., the normalized absorption q and the saturation parameter s on the behavior of the SN point $g = g_{SN}$ of the single LS branch in both one and two spatial dimensions. To this aim we perform one- and two-dimensional fold continuations for different q and s and our results are presented in Fig. 10.

Figure 10 (a) shows continuation of the folding point g_{SN} as a function of q , obtained for different values of s , while in panel (b) fold continuation of g_{SN} as a function of s , for different values of q , are presented. Dashed (solid) lines in both panels indicate one- (two-) dimensional continuation, respectively. Note that the two-dimensional folding point is always shifted to higher current values compared with the one-dimensional case, the overall evolution of the folding point g_{SN} remains the same. Furthermore, the behavior of g_{SN} with q and s follows the same trends as the homogeneous solution (cf. Sec. 2), including its asymptotic behavior in the

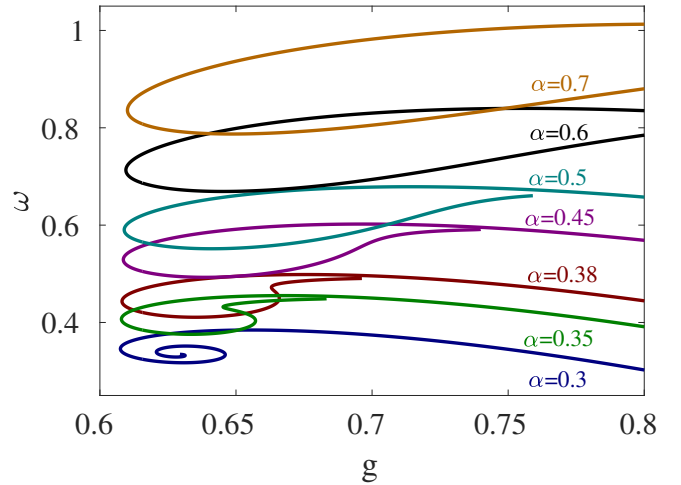


Figure 11. (Color online) One-dimensional bifurcation diagram of Eq. 9 in (g, ω) plane calculated for increasing values of α at fixed $\beta = 0.5$. For small α the branch of a single LS forms a spiral which unfolds for increasing α . Different colors correspond to different values of α . Other parameters are the same as in Fig. 2.

limit of large saturation and large absorption. That is, our predictions for the folding point evolution of the homogeneous solution hold for the folding point of the LS solution.

c. Unfolding of the spiral

Figure 11 shows the typical spiral shape obtained for the branch of a LS in the (g, ω) plane at low values of α . One can see that the spiral shape of the LS branch remains well preserved for small values of α (cf. Fig. 11 for $\alpha = 0.3$). However, for increasing α the morphology of the branch changes: Beyond a certain threshold, the end point of the spiral curve moves to higher gain values (see Fig. 11 for $\alpha = 0.35 \dots 0.5$), leading to the unfolding of the spiral ($\alpha = 0.6, 0.7$). There, the resulting branch bifurcates from the threshold $g = 1$, exhibits a fold at a certain g and continues towards higher gain values, i.e., it coexists with the upper sub-branch and always exhibits smaller ω . This branch morphology remains for ascending α as shown in Fig. 2.

d. Numerical simulation of the Haus Equation

We solved Eqs. (1-3) by adding two additional free parameters ω and v which correspond to the oscillation frequency and the drift velocity of the solution along the propagation axis. In other words, the round-trip of the LBs presents a small deviation with respect to the cold cavity round-trip time that corresponds to a drift v in the reference frame of the cold cavity where one takes a snapshot every round-trip time, see [15] for more details.

As such Eq. 1 is rewritten as

$$\partial_\sigma E = (O_1 + O_2) E \quad (\text{A.17})$$

with the two operators $O_{1,2}$ defined as

$$O_1 = \sqrt{\kappa} \left[\frac{1 - i\alpha}{2} G(r_\perp, z, \sigma) - \frac{1 - i\beta}{2} Q(r_\perp, z, \sigma) \right] + \sqrt{\kappa} - 1 + i\omega \quad (\text{A.18})$$

$$O_2 = \frac{1}{2\gamma^2} \partial_z^2 + (d + i) \Delta_\perp + v \partial_z \quad (\text{A.19})$$

The values of the free parameters (ω, v) are adapted during the time integration via a simple control loop allowing to determine the frequency by looking at the phase variation of the peak of the LB and the drift along the propagation axis of the intensity profile averaged over the transverse dimension(s). In particular, canceling the natural drift of the solution along the propagation axis by a proper value of v allows to maintain the position of the LB close to the center of the numerical domain.

We solved Eq. A.17 using a semi-implicit split-step method in which the spatial operator O_2 is evaluated in Fourier space. Denoting \tilde{O}_2 the differential operator in Fourier space, the update sequence reads

$$E_1 = E_n (1 + \Delta t \times O_1), \quad (\text{A.20})$$

$$E_2 = \mathcal{F}^{-1} \left[e^{\Delta t \times \tilde{O}_2} \mathcal{F}[E_1] \right], \quad (\text{A.21})$$

$$E_{n+1} = E_2 / (1 - \Delta t \times O_1). \quad (\text{A.22})$$

As the carrier variables G and Q are not depending on the slow time, since we exploited the long cavity limit, the operator O_1 can be obtained from the integration of Eqs. (2-3) knowing the pre-existing field intensity distribution and using Dirichlet boundary conditions at the beginning of the integration domain that reads

$$(G, Q)(r_\perp, z = 0) = (G_0, Q_0). \quad (\text{A.23})$$

We used a physical domain $\Omega_H = [-L_x, L_x] \times [-L_y, L_y] \times [-L_z, L_z]$ with $L_{x,y} = 160$ and $L_z = 3$ using a grid with $N_x \times N_y \times N_z$ mesh points and $N_{x,y,z} = 128$. Periodic boundary conditions are automatically imposed in both x, y directions, as a consequence of the differentiation in Fourier space. We applied standard dealiasing with a 2/3 rule to the Fourier operator. As the Fourier operator \mathcal{O}_2 is linear, no dealiasing is needed. As such, one has to put dealiasing into \mathcal{O}_1 every time one goes into the Fourier space and we apply the 2/3 rule in $\mathcal{F}[E_1]$ in Eq. 30 only.

The time step was $\delta t = 0.1$ which gives indistinguishable results for the LB parameters like energy, width, frequency and velocity as compared to smaller time steps. The main reason for this strong convergence property stems from the fact that around a steady state $O_1 \simeq 0$ while the spatial operator O_2 is obtained via exponential differencing and is therefore exact. As such, the remaining errors stems only from the operator splitting. It is proportional to a commutator that reads

$[1 \pm \Delta t \times O_1, e^{\Delta t \times \tilde{O}_2}] \simeq 0$ since $O_1 \simeq 0$ at steady state. A convergence analysis of the numerical method yielded the expected second-order accuracy. Finally, we added to the field equation white Gaussian noise with variance $\xi = 10^{-4}$ mainly to accelerate the escape from unstable solutions and to avoid the detection of false positive. The time integration was $\Delta \sigma = 3 \times 10^3$.

The numerical bifurcation diagrams were obtained by increasing g from a minimal value $g = 0.4$ up to $g = 1$ with a step of $\delta g = 2 \times 10^{-3}$. As initial conditions, we used a spherical solution $E_i(x, y, z) = E_0$ with (x, y, z) verifying the relation

$$\left(\frac{x}{L_x} \right)^2 + \left(\frac{y}{L_y} \right)^2 + \left(\frac{z}{L_z} \right)^2 < 1 \quad (\text{A.24})$$

with parameters $L_x = L_y = 10$, $L_z = 0.26$ and $E_0 = 1$. After an integration time of $\Delta \sigma$, if a stable LB solution is found, it is used as an initial condition for the next value of g . After the entire upward scan in g the solution branch is further extended via continuation downward from the first point that was found using the spherical IC. This methods allows to get a good approximation of the folding point limiting the branch at low values of g . However, during such “blind” parameters sweeps, a large fraction of the simulations consist in a dynamics in which the field goes down to $E = 0$ or the spatio-temporal profile explodes and invades the full numerical domain. As such, special flags were introduced to cut the time integration. This simple procedure diminishes the computation times by several orders of magnitudes. The scans along q were performed with a step $\delta q = 3 \times 10^{-2}$. Simulations were performed using 100 cores of Xeon E5 CPUs on a HPC cluster Bull B510.

The results of the scan in the (α, g) and (β, g) planes are presented in Fig. 12 where we represented the characteristics of the LBs, as for instance their FWHM in the transverse and longitudinal directions, the residual frequency and the velocity of propagation along the propagation axis. As mentioned in the main text, the stability region increases with larger values of α and smaller values of β .

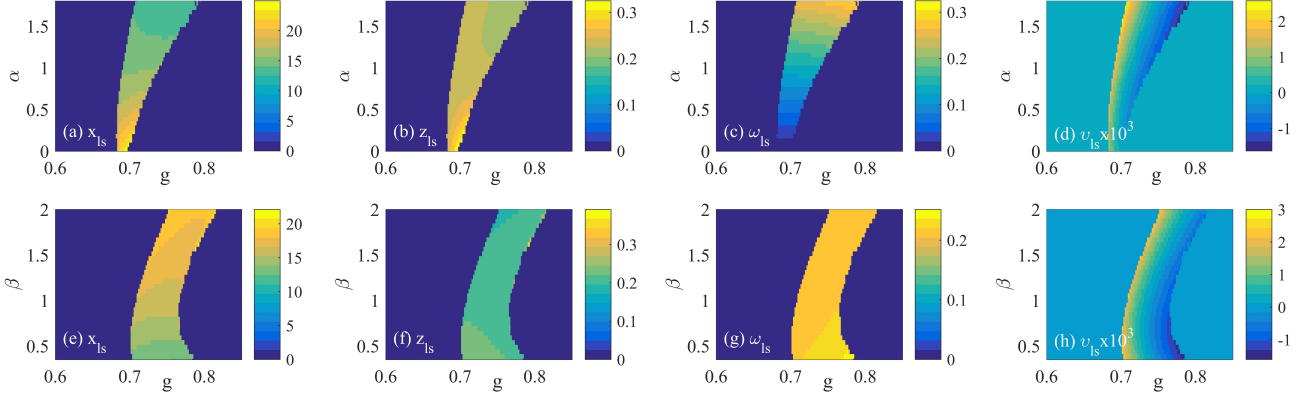


Figure 12. (Color online). Two-dimensional bifurcation diagrams showing the region of stable existence of the LBs by integrating the two-dimensional Haus equation Eqs. (1-3) as a function of the gain g and the parameters α (a) and β (b). We represent the FWHM in x (a, e), the FWHM in z (b, f) the frequency of the solution (c, g) and the drift velocity (d, h). As mentioned in the main text, the range of stability increases with α and reduces for small values of β in agreement with Fig. 4. Parameters are $(\gamma, \kappa, \Gamma, Q_0 d) = (40, 0.8, 0.04, 0.3, 10^{-2})$ and $\beta = 0.5$ (a-d), $\alpha = 1.5$ (e-h).

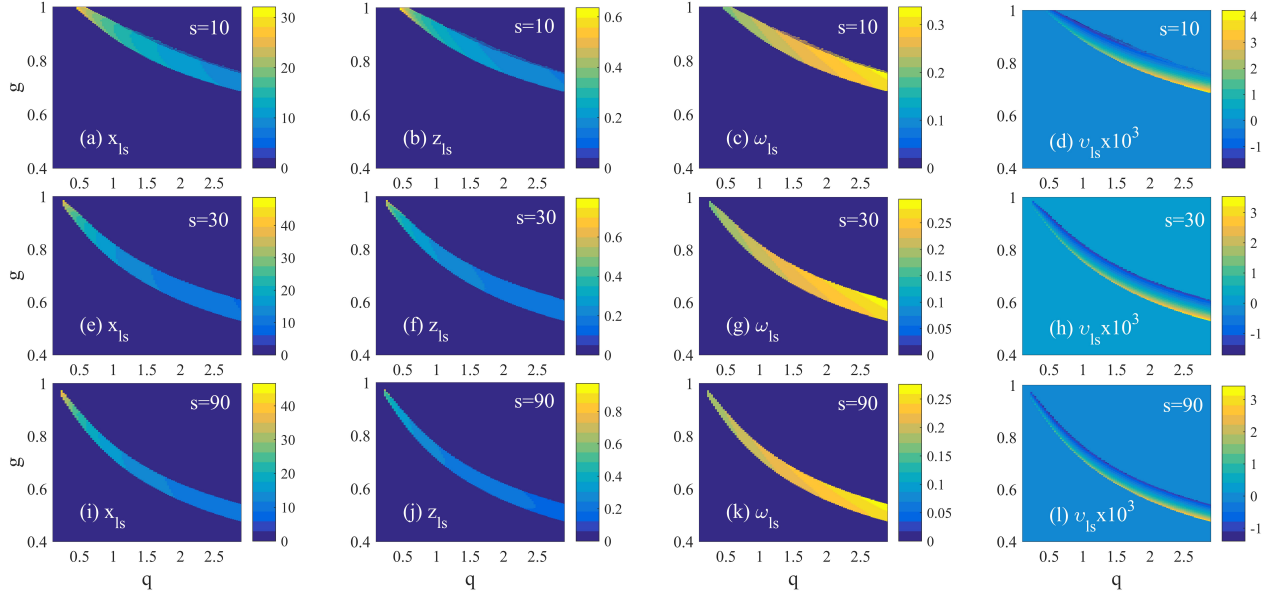


Figure 13. (Color online). Two-dimensional bifurcation diagram showing the region of stable existence of the LBs by integrating the two-dimensional Haus equation Eqs. (1-3) as a function of the gain g and the parameters α (a) and β (b). We represent the FWHM in x (a, e), the FWHM in z (b, f) the frequency of the solution (c, g) and the drift velocity (d, h). As mentioned in the main text, the range of stability increases with α and reduces for small values of β in agreement with Fig. 4. Parameters are $(\gamma, \kappa, \Gamma, Q_0 d) = (40, 0.8, 0.04, 0.3, 10^{-2})$ and $\beta = 0.5$ (a-d), $\alpha = 1.5$ (e-h).

-
- [1] Y. Silberberg, “Collapse of optical pulses,” *Opt. Lett.* **15**, 1282–1284 (1990).
 - [2] V. E. Zakharov, “Collapse of Langmuir Waves,” *Soviet Journal of Experimental and Theoretical Physics* **35**, 908 (1972).
 - [3] M. Tlidi and P. Mandel, “Space-time localized structures in the degenerate optical parametric oscillator,” *Phys. Rev. A* **59**, R2575–R2578 (1999).
 - [4] N. Veretenov, A. Vladimirov, N. Kaliteevskii, N. Rozanov, S. Fedorov, and A. Shatsev, “Conditions for the existence of laser bullets,” *Optics and Spectroscopy* **89**, 380–383 (2000).
 - [5] M. Brambilla, T. Maggipinto, G. Patera, and L. Columbo, “Cavity light bullets: Three-dimensional localized structures in a nonlinear optical resonator,” *Phys. Rev. Lett.* **93**, 203901 (2004).

- [6] L. Columbo, I. M. Perrini, T. Maggipinto, and M. Brambilla, “3d self-organized patterns in the field profile of a semiconductor resonator,” *New Journal of Physics* **8**, 312 (2006).
- [7] M. Marconi, J. Javaloyes, S. Balle, and M. Giudici, “How lasing localized structures evolve out of passive mode locking,” *Phys. Rev. Lett.* **112**, 223901 (2014).
- [8] H. A. Haus, “Mode-locking of lasers,” *IEEE J. Selected Topics Quantum Electron.* **6**, 1173–1185 (2000).
- [9] J. Javaloyes, “Cavity light bullets in passively mode-locked semiconductor lasers,” *Phys. Rev. Lett.* **116**, 043901 (2016).
- [10] N. N. Rosanov and G. V. Khodova, “Autosolitons in nonlinear interferometers,” *Opt. Spectrosc.* **65**, 449–450 (1988).
- [11] H. Uecker, D. Wetzel, and J. Rademacher, “pde2path - a matlab package for continuation and bifurcation in 2d elliptic systems,” *Numerical Mathematics: Theory, Methods and Applications* **7**, 58–106 (2014).
- [12] P. Genevet, S. Barland, M. Giudici, and J. R. Tredicce, “Cavity soliton laser based on mutually coupled semiconductor microresonators,” *Phys. Rev. Lett.* **101**, 123905 (2008).
- [13] M. Brambilla, L. A. Lugiato, F. Prati, L. Spinelli, and W. J. Firth, “Spatial soliton pixels in semiconductor devices,” *Phys. Rev. Lett.* **79**, 2042–2045 (1997).
- [14] M. Marconi, J. Javaloyes, S. Balle, and M. Giudici, “Passive mode-locking and tilted waves in broad-area vertical-cavity surface-emitting lasers,” *Selected Topics in Quantum Electronics, IEEE Journal of* **21**, 85–93 (2015).
- [15] J. Javaloyes, P. Camelin, M. Marconi, and M. Giudici, “Dynamics of localized structures in systems with broken parity symmetry,” *Phys. Rev. Lett.* **116**, 133901 (2016).
- [16] G. New, “Pulse evolution in mode-locked quasi-continuous lasers,” *Quantum Electronics, IEEE Journal of* **10**, 115 – 124 (1974).
- [17] A. G. Vladimirov and D. Turaev, “Model for passive mode locking in semiconductor lasers,” *Phys. Rev. A* **72**, 033808 (2005).
- [18] T. Dohnal, J. Rademacher, H. Uecker, and D. Wetzel, “pde2path-version 2.0: faster fem, multi-parameter continuation, nonlinear boundary conditions, and periodic domains-a short manual,” arXiv:1409.3119 (2014).
- [19] H. Uecker, D. Wetzel, and J. Rademacher, “pde2path - a matlab package for continuation and bifurcation in 2d elliptic systems,” *Numerical Mathematics: Theory, Methods and Applications* **7**, 58–106 (2014).
- [20] R. Seydel, *Practical bifurcation and stability analysis*, Interdisciplinary Applied Mathematics (Springer-Verlag New York, 2010), 3rd ed.
- [21] Y. A. Kuznetsov, *Elements of Applied Bifurcation Theory, Second Edition*, Applied Mathematical Sciences (Springer-Verlag, 1998), 2nd ed.
- [22] A. G. Vladimirov, S. V. Fedorov, N. A. Kaliteevskii, G. V. Khodova, and N. N. Rosanov, “Numerical investigation of laser localized structures,” *Journal of Optics B: Quantum and Semiclassical Optics* **1**, 101 (1999).
- [23] T. Dohnal, J. Rademacher, H. Uecker, and D. Wetzel, “pde2path-version 2.0: faster fem, multi-parameter continuation, nonlinear boundary conditions, and periodic domains-a short manual,” arXiv:1409.3119 (2014).
- [24] A. G. Vladimirov, N. N. Rozanov, S. V. Fedorov, and G. V. Khodova, “Bifurcation analysis of laser autosolitons,” *Quantum Electronics* **27**, 949 (1997).
- [25] A. G. Vladimirov, N. N. Rozanov, S. V. Fedorov, and G. V. Khodova, “Analysis of the stability of laser solitons,” *Quantum Electronics* **28**, 55 (1998).